

Compression for Smooth Shape Analysis

V. Estellers
TUM

virginia.estellers@tum.de

F.R. Schmidt
TUM, BCAI

frank.schmidt12@de.bosch.com

D. Cremers
TUM

cremers@tum.de

Abstract

Most 3D shape analysis methods use triangular meshes to discretize both the shape and functions on it as piecewise linear functions. With this representation, shape analysis requires fine meshes to represent smooth shapes and geometric operators like normals, curvatures, or Laplace-Beltrami eigenfunctions at large computational and memory costs.

We avoid this bottleneck with a compression technique that represents a smooth shape as subdivision surfaces and exploits the subdivision scheme to parametrize smooth functions on that shape with a few control parameters. This compression does not affect the accuracy of the Laplace-Beltrami operator and its eigenfunctions and allow us to compute shape descriptors and shape matchings at an accuracy comparable to triangular meshes but a fraction of the computational cost.

Our framework can also compress surfaces represented by point clouds to do shape analysis of 3D scanning data.

1 Introduction

Many shape analysis tasks describe shapes as smooth manifolds and analyze them with respect to their geometry in terms of normals, curvatures, and geodesics that require accurate estimates of first- and second-order derivatives over the shape to compute tangent spaces, the Riemannian metrics, or Laplace-Beltrami operators [28, 18, 34, 19]. When the surface is represented as a mesh or point cloud, these differential operators can only be computed approximately at large memory and computational costs.

Once these differential operators have been used to compute normals or metrics, most of the high resolution information is discarded by operating only with the leading

eigenfunctions of the Laplace-Beltrami operator necessary to estimate geodesics [7], compute shape descriptors [1, 28, 18, 19] or shape matches [25] with tractable problem sizes. This creates a paradox, as shapes are first discretized with fine meshes or large pointclouds to estimate high-dimensional shape operators that are mostly discarded to analyze the shape. This paradox appears because we only need large meshes or dense pointclouds to discretize accurate differential operators over the shape, not for shape analysis.

We propose a paradigm shift that avoids this paradox by representing a shape with a subdivision surface [24] that parametrizes the surface with a small set of smooth base functions. Differentiability is then intrinsic to the shape representation and does not require large bases to compute principal curvatures, wave-kernel signatures, or Laplace-Beltrami eigenfunctions. Subdivision surfaces are a generalization of splines to surfaces of arbitrary topology that provide set of base functions to compactly parametrize the surface as well as smooth functions over it. As a result, subdivision surfaces provide a compressed shape representation well suited to shape analysis.

Our first contribution (Section 3) is a method to estimate a subdivision surface from the triangular meshes common in shape analysis[2]. This kind of manifold meshes, however, are far from the meshes or pointclouds obtained from range measurements or computer-vision models. As these low-level representations proliferate, they create a challenge for shape analysis to adapt to the characteristics of raw data (irregular surface sampling, noise, and outliers) that cause havoc in the estimation of differential operators. Up until now, raw measurements have been largely ignored in shape analysis by estimating a mesh representation from a pointcloud and performing analysis on this representation. This avoids dealing with noise and outliers but ignores the direct measurements and makes

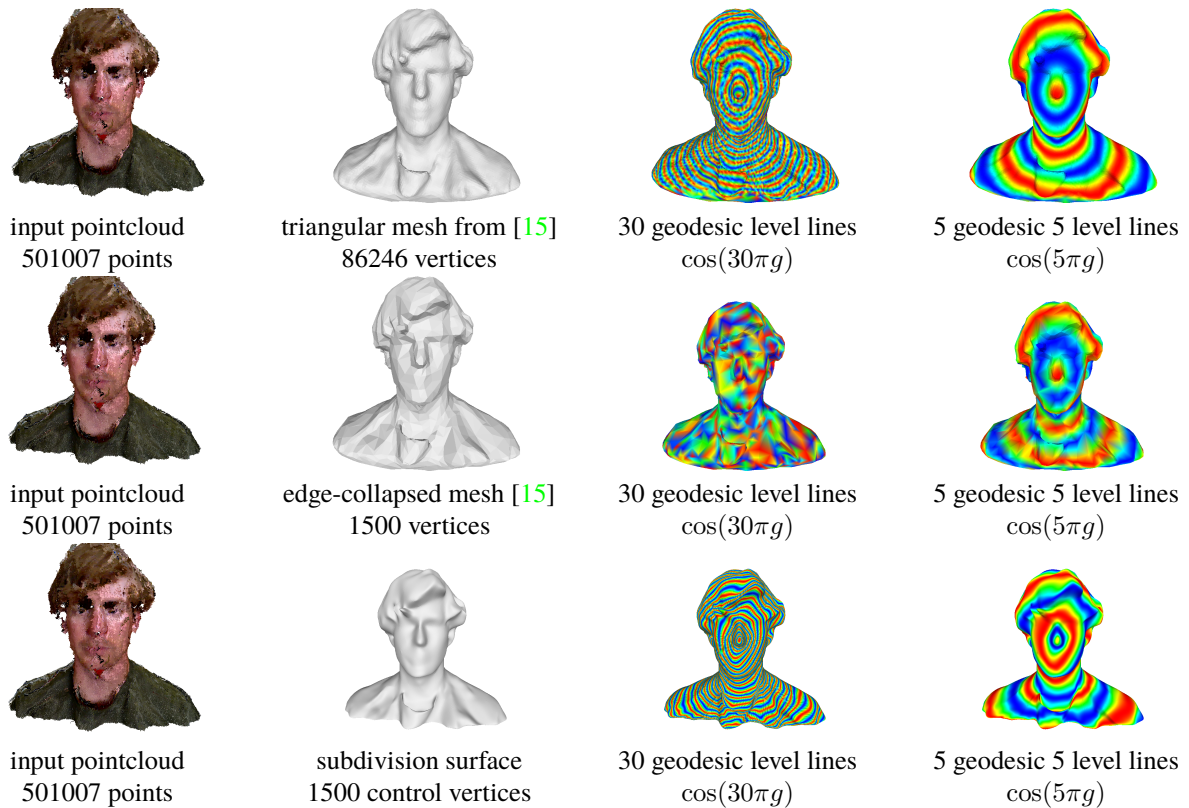


Figure 1: Computation of approximate geodesic g with different surface representations by the Heat method [7]. Column 1: input Kinect pointcloud. Column 2: representation of the surface with a high-resolution mesh obtained with Poisson reconstruction [15] (row 1), a low-resolution triangular mesh obtained by quadratic edge collapse [9] of the high-resolution mesh (row 2), and with our subdivision surface (row 3). Columns 3 and 4: level lines of the geodesic visualized as $\cos(\varpi g)$. Our subdivision surface is comparable to the surface obtained by Poisson reconstruction and faithfully represent geodesics at low and high resolution with 2% of vertices. Compressing the Poisson mesh by edge collapse loses all the small scale details of the surface and its geodesic, as highlighted by high-frequency level lines of the geodesic.

shape analysis dependent on the model used to estimate the surface.¹ For this reason, our second contribution is a robust method that fits a subdivision surface to a noisy pointcloud and estimates the geometric operators required to do shape analysis on it. Our model is robust to both noise and outliers in the pointcloud and to erroneous correspondences between the input points and the subdivision

¹Least-squares models [15, 4], for instance, oversmooth surface edges and require less eigenfunctions to match than the ℓ_1 models [31, 8] that emphasize corners.

surface. This is a critical aspect of fitting a parametric surface to raw data without developing the non-manifold artifacts that prevent shape analysis.

Our third contribution is a fast optimization algorithm (Section A) that combines a sequential quadratic approximation with a good initialization strategy. This is important because fitting a subdivision surface is not a convex problem and vanilla initializations [13] oversmooth the surface to avoid small-scale local minima and prevent self-intersections.

Our fourth contribution (Section 2) describes how to accurately compute many shape operators with a subdivision surface. We focus on Laplace-Beltrami operator, wave kernel signatures [1], approximate geodesics [7] and prove its efficacy in the full-pipeline task of shape matching [25]. Our experiments show state-of-the-art performance at a fraction of the memory requirements of shape representations with triangular meshes.

2 Smooth Shapes

In this paper, a *3D shape* is a smooth², compact oriented surface $S \subset \mathbb{R}^3$ without boundaries.

For computational purposes, shapes are usually discretized by a mesh $\mathbf{M} = (V, F)$ in terms of two matrices: the i -th row of $V \in \mathbb{R}^{n \times 3}$ stores the location of the i -th vertex of the mesh, while each row of $F \in \mathbb{N}^{m \times k}$ stores the indices of the vertices of a face of \mathbf{M} . We focus on quad meshes with $k = 4$.

In shape analysis, quad meshes usually discretize a smooth surfaces as a piecewise C^1 surface that is not smooth. Subdivision surfaces, on the other hand, only use meshes to discretize the domain of a smooth surface parametrization. To formally introduce this parametrization, we first revisit the topological space associated to a quad mesh and show how it can be used to define a smooth subdivision parametrization.

2.1 Meshes – Piecewise Bilinear Surfaces

The regular quad mesh parametrization of a surface $S_{\mathbf{M}}$ consists of quadrilaterals “glued” together along their edges. Each quadrilateral in $S_{\mathbf{M}}$ is modeled by a bilinear patch that fits the four vertices of a facet in \mathbf{M} and is glued to its neighboring facets. This topological gluing extends the independent parametrization of each quadrilateral to the whole mesh and is formalized by the topological space, $\mathcal{T}_{\mathbf{M}}$, that defines the domain of the parametrization [14].

Formally, given a quad mesh $\mathbf{M} = (V, F)$, the topological space $\mathcal{T}_{\mathbf{M}}$ is defined by a set of quads that is indexed by the mesh facets $\mathcal{I}_F = \{1, \dots, m\}$ and glued together by the equivalence relation \sim , that is $\mathcal{T}_{\mathbf{M}} := \square \times \mathcal{I}_F / \sim$.

² We call a C^1 object smooth if it is C^2 except for a finite subset. This differs from the mathematical notion, which identifies smoothness with C^∞ .

The *reference quad* $\square = [0, 1] \times [0, 1]$ parametrizes each quadrilateral patch while the equivalence relation \sim connects neighboring faces along their common edge.

A parametrization of the surface is then obtained by defining a piecewise bilinear function

$$B_{\mathbf{M}}^i: \mathcal{T}_{\mathbf{M}} \rightarrow \mathbb{R}$$

for each vertex in $x_i \in \mathcal{T}_{\mathbf{M}}$ satisfying $B_{\mathbf{M}}^i(x_j) = \delta_{ij}$. The resulting parametrization

$$\Phi_{\mathbf{M}}: \mathcal{T}_{\mathbf{M}} \rightarrow S_{\mathbf{M}} \subset \mathbb{R}^3$$

defines the piecewise C^1 surface $S_{\mathbf{M}} := \Phi_{\mathbf{M}}(\mathcal{T}_{\mathbf{M}})$ by bilinear interpolation

$$\Phi(u) = \sum_{i=1}^n B_{\mathbf{M}}^i(u) \cdot v_i.$$

With such a piecewise C^1 parametrization, Riemannian quantities like the first or second fundamental form can only be approximated and need large meshes with small quadrilaterals for accurate approximations. This limits their use in real-time applications and calls for other shape representations.

2.2 Smooth Subdivision Surfaces

A subdivision surface represents a smooth surface S by a coarse control mesh $\mathbf{M}^0 = (V^0, F^0)$ and a subdivision scheme. The subdivision scheme transforms a mesh $\mathbf{M}^k = (V^k, F^k)$ into a finer mesh \mathbf{M}^{k+1} such that if we start with $\mathbf{M}^0 := (V, F)$, we obtain the smooth surface as the limit of iterating subdivision ad infinitum:

$$S = \lim_{k \rightarrow \infty} S_{\mathbf{M}^k}.$$

In this paper we follow the Catmull-Clark subdivision scheme $\mathbf{M}^k \mapsto \mathbf{M}^{k+1}$ consisting of two steps: First, the topology of the new mesh \mathbf{M}^{k+1} is defined by subdividing each quad in $\mathcal{T}_{\mathbf{M}^k}$ into its four quadrants that define four adjacent facets in $\mathcal{T}_{\mathbf{M}^{k+1}}$. Second, the location of each vertex of the new mesh \mathbf{M}^{k+1} is computed as a linear combination of the positions of the nearby vertices. Figure 2 illustrates this subdivision process.

This produces a compressed surface representation because the topology of \mathbf{M}^{k+1} is completely determined by

the topology of \mathbf{M}^k . Similarly, the space of bilinear functions over $\mathcal{T}_{\mathbf{M}^{k+1}}$ created by subdivision is determined by the space of bilinear functions over $\mathcal{T}_{\mathbf{M}^k}$. This means that we can parametrize the i -th function created by subdivision $B_{\mathbf{M}^{k+1}}^i$ over the domain $\mathcal{T}_{\mathbf{M}^k}$, and by induction over $\mathcal{T}_{\mathbf{M}}$, instead than $\mathcal{T}_{\mathbf{M}^{k+1}}$. We denote these functions $B_{\mathbf{M}}^{k,i} : \mathcal{T}_{\mathbf{M}} \rightarrow \mathbb{R}$ and use them to parametrize the surface $S_{\mathbf{M}^k} = \Phi_{\mathbf{M}}^k(\mathcal{T}_{\mathbf{M}})$ as a function of the vertices of \mathbf{M}^k .

In the second step, the position of the vertices of \mathbf{M}^{k+1} are computed as linear combination of the positions of the vertices of \mathbf{M}^k . The weights of this linear combination are organized into a subdivision matrix $\hat{A}_k \in \mathbb{R}^{n_k \times n_{k-1}}$ that computes the position of the vertices of \mathbf{M}^k as

$$V_k = \underbrace{\hat{A}_k \dots \hat{A}_1}_{A_k \in \mathbb{R}^{n_k \times n}} V = A_k V.$$

Using this linear dependency, we can parametrize a surface approximation $S_{\mathbf{M}^k}$ resulting from k subdivisions directly over $\mathcal{T}_{\mathbf{M}}$ as follows:

$$\Phi_{\mathbf{M}}^k(u) = \sum_{i=1}^{n_k} B_{\mathbf{M}}^{k,i}(u) (A_k V)_i = \sum_{j=1}^n \sum_{i=1}^{n_k} B_{\mathbf{M}}^{k,i}(u) A_{k,ij} v_j$$

By iterating this process, the subdivision surface of the limit

$$S = \lim_{k \rightarrow \infty} S_{\mathbf{M}^k}$$

can be formulated as a limit of functions defined over the topological space $\mathcal{T}_{\mathbf{M}}$. Evaluating the limit surface at the location of the vertex thus amounts to computing the base functions

$$\Phi_j := \lim_{k \rightarrow \infty} \sum_{i=1}^{n_k} B_{\mathbf{M}}^{k,i} \cdot A_{k,ij}.$$

The existence of this limit and the smoothness of the limit functions is guaranteed by the subdivision scheme. All the *limit base functions* Φ_j are compactly supported because the subdivision rules act locally and converge to spline basis functions. This equivalence provides analytic derivatives and fast evaluation techniques [29] for smooth functions or tangent vectors defined over the surface and makes subdivision surfaces well-suited for shape analysis.

We focus on Catmull-Clark subdivision [6] for simplicity. This scheme ensures the existence and C^2 smoothness of the basis functions everywhere except at extraordinary vertices (vertices with valence different than four).

This scheme is designed for control grids with quadrilateral connectivity, but our compression generalizes to any subdivision schemes that parametrizes C^2 surfaces.

3 Robust Fitting Model

We formulate the problem of fitting a subdivision surface S to a set of surface samples $\mathbf{P} = \{p_1, \dots, p_N\}$ and a set of normals $\mathbf{T} = \{t_1, \dots, t_N\}$ as the minimization problem:

$$\min_S E(S) := \underbrace{\text{dist}(S, \mathbf{P})}_{\text{Point Fit}} + \alpha \cdot \underbrace{\mathcal{T}(S, \mathbf{T})}_{\text{Tangent Fit}} + \underbrace{\beta \cdot R(S)}_{\text{Regularization}}, \quad (1)$$

where $\alpha, \beta \geq 0$ are model parameters. The different terms take different information into account: $\text{dist}(S, \mathbf{P})$ fits the surface S to the points \mathbf{P} , $\mathcal{T}(S, \mathbf{T})$ matches the tangent plane of S to the normal information \mathbf{T} , and $R(S)$ regularizes the discrete representation of S to avoid degenerate faces in \mathbf{M} . If no normal information is provided, $\alpha = 0$.

Point Fit

Let $\mathcal{D}_S(p) = \min_{s \in S} \|s - p\|$ denote the Euclidean distance between a point $p \in \mathbb{R}^3$ and the compact surface S , we define the *point fit energy* as

$$\text{dist}(S, \mathbf{P}) := \sum_{j=1}^N \mathcal{D}_S(p_j)^q = \sum_{j=1}^N \min_{u_j \in \mathcal{T}_{\mathbf{M}}} \|\Phi(u_j) - p_j\|^q.$$

Using the q -th power of the distance with $q \in (1, 2)$, instead of the common squared distance, makes our model robust to outliers and scanning artifacts in the input samples. The minimization in u_1, \dots, u_N results from the parametric representation of the surface $S = \Phi(\mathcal{T}_{\mathbf{M}})$ and introduces a large number of additional variables over which the objective function is not convex. We avoid the optimization of the correspondence parameters u_1, \dots, u_N by using a second-order approximation of the squared distance function to a surface in Section A.

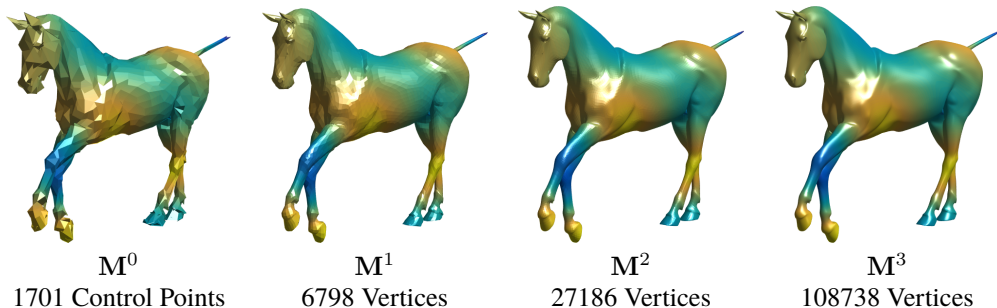


Figure 2: Different subdivision levels M^k of Catmull-Clark subdivision scheme applied to a control mesh and a smooth function defined over the mesh (its 18-th Δ eigenfunction). M^3 is already a good approximation of the smooth surface $S = M^\infty$.

Tangent Fit

To obtain a surface that also matches the normals, we include the *tangent energy*

$$\mathcal{T}(S, \mathbf{T}) = \sum_{j=1}^N |\langle t_j, \partial_1 \Phi(u_j) \rangle|^q + |\langle t_j, \partial_2 \Phi(u_j) \rangle|^q, \quad (2)$$

where t_j is the input surface normal at point p_j and $\partial_i \Phi(u_j)$ the i -th base vector of the tangent space $T_{\Phi(u_j)} S$. Each term in \mathcal{T} aligns the tangent space of the subdivision surface in the direction orthogonal to the sample normal. This penalty is designed to be independent of the orientation of the normals to account for noisy point clouds where estimating consistent normal orientations is prone to fail. The ℓ_q -norm makes this term robust to noise and outliers in the normals and the correspondence parameters u_1, \dots, u_N .

Regularization

The regularizer $R(S)$ penalizes the squared distance between the vertices of the mesh M incident to the same quad. This keeps the size and shape of the quads regular and avoids skewed elements that cause instabilities in finite-element computations. The regularizer is thus a simple quadratic penalty that can be described by a sparse matrix R that has a row for each edge in the mesh with entries ± 1 at the columns of the vertices incident to the edge. We choose this regularizer for its simplicity.

3.1 Initialization and Surface Topology

A major challenge of fitting any explicit parametrization to a set of points is the lack of convex formulations for the optimization problem. Non-convexity introduces the difficulty of finding a suitable initialization that leads to a *good* local minimum. It is an important step of the algorithm that conditions the topology of the surface.

By parameterizing S with a subdivision surface, our optimization problem is formulated in terms of the control mesh $M = (V, F)$. To avoid solving a combinatorial problem, we fix the topology of the control mesh, and thus the topology of the surface, and only optimize for the location of the vertices V . We design the control mesh to satisfy two properties: it determines a surface with the same topology as the input data, and it has a small number of vertices to represent the surface compactly. Depending on the input data, we apply different methods to obtain a good initialization.

If the point samples \mathbf{P} are the vertices of a mesh \overline{M} , the topology of the surface is already encoded by the mesh. Without loss of generality, we assume that \overline{M} is a triangular mesh without boundaries and use quadratic edge-collapse [9] to reduce the number of vertices in the mesh and preserve the surface topology. We then transform this triangular mesh into a quad mesh by solving a perfect matching problem that pairs triangles of the collapsed mesh to create quads [27]. For each edge e , let $\alpha_1(e), \dots, \alpha_4(e) \in \mathbb{S}^1$ be the angles of the quad that results from removing e and $\eta(e) \in \mathbb{S}^1$ the angle between the normals of the triangles incident to e . We set the cost

of removing an edge e to

$$c(e) = \begin{cases} \frac{1}{4} \sum_{i=1}^4 d(\alpha_i(e), \frac{\pi}{2})^2 + \tan(\eta(e))^2 & \text{if } |\eta(e)| < \frac{\pi}{2} \\ \infty & \text{if } |\eta(e)| \geq \frac{\pi}{2}. \end{cases}$$

to assign infinity costs to edges that connect strongly bent triangles ($\eta(e) > \frac{\pi}{2}$) or edges that would create quads with straight or reflex angles. The cost favors rectangular quads to obtain a subdivision surface where finite-element computations are accurate and numerically stable. We solve the perfect matching and find the quad mesh with minimum cost with the *Blossom V* method [16].

When the input is a point cloud, we use an implicit representation to estimate the topology of the surface from the point samples and only then extract a control mesh. Estimating first the topology of the surface with an implicit representation avoids explicitly handling topology changes during the compression process. We use the popular Poisson reconstruction [15] for simplicity but other techniques like voxel hashing work well. From this implicit representation, we extract a closed triangular mesh with marching cubes [21] and create a compact quad mesh with the collapse and blossom techniques described for meshes.

4 Efficient Optimization

Our optimization algorithm exploits the properties of subdivision surfaces, namely, the compact support of the basis functions and the ability to analytically evaluate its geometry, with a sequential quadratic program that is more efficient than the gradient-based algorithms proposed by [5, 12, 13]. We solve (9) as a sequence of convex problems

$$v^{m+1} \leftarrow \min_v v^\top (Q^m v - b) \quad (3)$$

that approximate the original energy around the current surface estimate by a least-squares problem. The approximation is derived from the surface geometry, while the sparsity of Q^m results from compactness of the subdivision basis.

We follow a *Majorize-Minimize* (MM) principle to minimize $E(S)$ by iterating two steps until convergence. The first step finds an upper envelop of the objective function

$E(S|S_0) \geq E(S)$ that coincides with E at S_0 . We derive an upper envelop of the data and tangent fits from the inequality

$$|d|^q \leq \frac{q}{2} |d_0|^{q-2} d^2 + (1 - \frac{q}{2}) |d_0|^q \quad \forall d_0 \neq 0, q \in [1, 2].$$

The second step of the MM algorithm minimizes the upper envelop the upper envelop and drives the value of the original function downwards by solving

$$S^{m+1} \leftarrow \min_S E(S|S^m).$$

In our case, the envelop

$$E(S|S^m) = \sum_{j=1}^n w_j^m \mathcal{D}_S(p_j)^2 + \sum_{i=1}^2 \alpha_{ij}^m \langle t_j, \partial_i \Phi^m(u_j) \rangle^2 + \beta R(S)$$

defines a weighted least-squares problem where the weights w_j^m and α_{ij}^m are determined by the MM principle

$$w_j^m = \frac{q}{2} \mathcal{D}_{S^m}(p_j)^{q-2} \quad \alpha_{ij}^m = \frac{\alpha q}{2} |\langle t_j, \partial_i \Phi^m(u_j) \rangle_{\epsilon}^{q-2}.$$

To simplify the minimization step of MM, we approximate $\mathcal{D}_{S^m}(\cdot)^2$ with a quadratic function that parametrizes the squared distance to a surface in terms of its geometry as follows:

$$\mathcal{D}_S^2(x) \approx (x - p)^\top \left[\frac{d \cdot \tau_1 \tau_1^\top}{d + \rho_1} + \frac{d \cdot \tau_2 \tau_2^\top}{d + \rho_2} + \nu \nu^\top \right] (x - p),$$

where p is a point on the surface S close to x (but not necessarily the projection of x onto S), $d := \|x - p\|$ is the signed distance from x to this point, and ρ_i, τ_i, ν are the principal curvature radii, the principal curvature directions and the normal to the surface at p . This approximation is due to [26] and coincides with the second order Taylor approximation within the radius of curvature of the surface at p , where it can be relaxed into a positive definite quadratic form by taking the absolute values of d, ρ_1, ρ_2 .

Incorporating this approximation into the upper envelop corresponds to using a quasi-Newton algorithm for optimizing jointly the control vertices of the subdivision surface and the parametric coordinates of the surface point closest to x [32, 20]. The approximation let us thus work with approximate correspondences between surface samples and input points, instead of explicitly finding the correspondences by solving a larger optimization problem.

It also makes our model robust to erroneous correspondences by taking into account their approximate nature in the objective function. The approximation, however, can affect the majorizing property and puts our algorithm into the category of sequential quadratic programs instead of MM algorithms.

The combination of the MM upper envelope with the quadratic approximation of the squared distance to S reduces to weighted least-squares problems in the vertices V (c.f. Appendix) that we solve efficiently with conjugate gradient solver warm-started with the solution of the previous MM minimization step.

After optimizing V at iteration m , we update the parameter values U where we approximate the squared distance to the surface by sampling the surface $S^m = \Phi^m(\mathcal{T}_M)$ uniformly and creating a kd-tree from these samples to find the parameter of the sample closest to each input point. This results in an efficient algorithm that avoids the slow convergence rates of coordinate descent algorithms and the large optimization problems of the Levenberg-Marquard solvers advocated by [5, 12, 13].

5 Smooth Shape Analysis

We have showed how to obtain smooth shapes from non-smooth input data like point clouds or meshes. We now show how to do *smooth shape analysis* with a subdivision surface S . To this purpose, we focus on the computation of the Laplace-Beltrami operator and its eigenfunctions and use them to match shapes, compute shape descriptors, and approximate geodesics.

5.1 Laplace-Beltrami-Operator

Given a smooth shape S , the Laplace-Beltrami-Operator Δ maps a twice continuously differentiable function $g \in C^2(S)$ to a continuous function

$$\Delta(g): S \rightarrow \mathbb{R},$$

If g satisfies Neumann boundary conditions, then Stokes' theorem

$$\int_S \Delta g \cdot h \, dx = \int_S \langle \nabla g, \nabla h \rangle \, dx$$

defines a weak formulation of Δ for Sobolev functions $g \in H^1(S)$. The Galerkin method uses this identity to define a discretization of Δ in the ansatz space $H_n^1(S)$ spanned by Sobolev functions $\Phi_1, \dots, \Phi_n \in H^1(S)$.

Using $H_n^1(S)$ as test space, g, h and Δg are represented by vectors $\alpha, \beta, \gamma \in \mathbb{R}^n$ as follows

$$g = \sum_{i=1}^n \alpha_i \Phi_i \quad h = \sum_{i=1}^n \beta_i \Phi_i \quad \Delta g = \sum_{i=1}^n \gamma_i \Phi_i$$

and the weak formulation of Δ in $H_n^1(S)$ reads

$$\langle \gamma, \beta \rangle_{D_0} = \langle \alpha, \beta \rangle_{D_1} \quad \forall \beta \in \mathbb{R}^n. \quad (4)$$

The Laplace-Beltrami operator in $H_n^1(S)$ thus depends on the mass and stiffness matrices $D_0, D_1 \in \mathbb{R}^{n \times n}$ whose entries

$$(D_0)_{ij} = \int_S \Phi_i \cdot \Phi_j \, dx \quad (D_1)_{ij} = \int_S \langle \nabla \Phi_i, \nabla \Phi_j \rangle \, dx.$$

compute the scalar product of functions and tangent vectors in the surface S .

From (4), the Laplace-Beltrami operator in $H_n^1(S)$ can be parametrized by the matrix $D_2 := D_0^{-1} D_1$. This matrix has a non-negative spectrum and its eigenvector discretizes the eigenfunctions of the operator Δ in $H_n^1(S)$. Indeed, if $v \in \mathbb{R}^n$ is an eigenvector of D_2 with eigenvalue λ , then $g_v = \sum_{i=1}^n v_i \Phi_i$ is an eigenfunction of Δ with eigenvalue λ in $H_n^1(S)$.

To particularize this construction to functions defined on a subdivision surface S , we consider the mapping

$$X(u, f) = \sum_{i=1}^n \Phi_i(u, f) v_i$$

that parametrizes the surface as a linear combination of n limit basis functions Φ_1, \dots, Φ_n and n mesh vertices v_1, \dots, v_n . Similarly, we can parametrize Sobolev functions over the surface $g \in H^1(S)$ by n scalar values $g_1, \dots, g_n \in \mathbb{R}$ with a mapping

$$g: S \rightarrow \mathbb{R} \quad (5)$$

$$\sum_{i=1}^n \Phi_i(u, f) \cdot v_i \mapsto \sum_{i=1}^n \Phi_i(u, f) \cdot g_i \quad (6)$$

that depends on each basis function Φ_i twice, once to describe the function g and once to describe the function

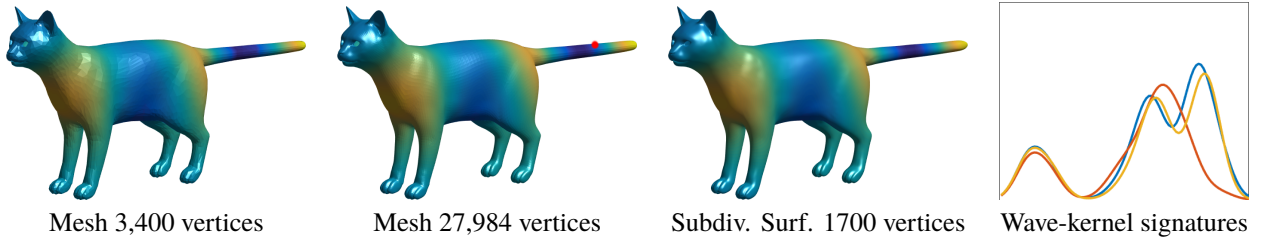


Figure 3: 12th Δ -eigenfunction and wave-kernel signature of the a surface point in red computed with fine (blue line) and coarse triangular meshes (red line) and a subdivision surface (yellow). The subdivision surface obtains a wave signature comparable to the fine mesh while the signature of the coarse mesh lacks detail.

domain S . As a result, the gradient of a surface function is

$$\nabla g(X(u, f)) = JX(u, f)(G^{-1}(u, f) \sum_{i=1}^n \nabla \Phi_i(u, f) \cdot g_i),$$

where JX is the Jacobian of the surface mapping X with respect to u .

When we use this parametrization to compute the mass and stiffness matrix, we need to evaluate the first fundamental form of S at a point $x \in S$ explicitly. Let $f \in \mathcal{I}_F$ be an arbitrary face index, then the first fundamental form at surface point $X(u, f)$ is

$$G(u, f) = JX(u, f)^\top JX(u, f). \quad (7)$$

We compute the surface integrals in the mass and stiffness matrices by pulling-back the integrand to the reference quad as follows:

$$\int_S g(s) ds = \sum_{f \in \mathcal{I}_F} \int_{\square} g \circ X(u, f) \sqrt{\det G(u, f)} du$$

We can compute the integral over the quad with arbitrary accuracy with high-order quadrature approximations. Experimentally, we obtain reliable mass and stiffness matrices with simple 3×3 Gaussian quadrature.

Note that when the subdivision surface S is derived from a control mesh with n vertices, $D_0, D_1, D_2 \in \mathbb{R}^{n \times n}$. An eigenfunction g_v of Δ is then obtained by solving an $n \times n$ generalized eigen problem and by parameterizing $g_v = \sum_{i=1}^n v_i \Phi_i$. In our figures, we use the refined \mathbf{M}^k mesh and the refined eigenfunction g_v^k for visualization. That is, g_v^k is not derived from the huge mass and stiffness matrices of \mathbf{M}^k but from the projection of $g_v \in C^1(S)$ onto the mesh \mathbf{M}^k .

5.2 Geodesic Distances

The classic approach to computing the geodesic distance χ to a surface point $S(u_0)$ is to solve the eikonal equation

$$\|\nabla \chi\| = 1 \quad (8)$$

subject to boundary conditions $\chi(u_0) = 0$. This results in a nonlinear hyperbolic PDE that is computationally expensive to solve. To alleviate the computational burden, [7] proposes a method to approximately solve (8) in terms of the Heat equation. This method first computes a function $f \in H^1(S)$ whose gradient is parallel to $\nabla \chi$ by integrating the Heat flow $\dot{f} = \Delta f$. It then approximates $\nabla \chi$ by the vector field $X = -\frac{\nabla f}{\|\nabla f\|}$ by observing that $\nabla \chi$ is parallel to ∇f and has unit norm as a result of (8). The method then finds an approximate χ by minimizing $\int_S \|\nabla \chi - X\|^2$ through its Euler-Lagrange equation $\Delta \chi = \nabla \cdot X$. As all the computations are formulated in terms of the Heat kernel Δ , the method can be directly use to compute approximate geodesics in our subdivision surface framework. We refer to [7] for the details of the method.

6 Related Work

Subdivision surfaces are a standard representation of shapes in computer graphics and animation, but they have largely been neglected in vision due to the challenges of working with noisy measurements that favor convex formulations and implicit representations.

Computer graphics techniques fit a subdivision surface by minimize the sum of squared distances between the

subdivision surface and the vertices of a clean and regular mesh [11, 22]. Research has focused into efficient ways of minimizing this non-convex energy by gradient-based techniques [35], quasi-Newton methods [23, 32, 20], and sequential convex programming [23, 17]. A very effective approach iteratively approximates the squared distance to the surface with a quadratic penalty [26] and minimizes the resulting convex energy. Our method adapts this strategy to the robust energies necessary to fit a surface to noisy data and outperform the squared distance penalty of [23] in three points: 1) We use robust data terms to account for noise and outliers in the input data. A robust energy also reduces the effects of errors in the correspondences (between input samples and the surface point closest them) and the quadratic distance approximation. This improves the accuracy of the surface independently of the noise present in the data, as our experiments show. 2) We use a second-order approximation to the squared distance function, instead of the first order of [23], to take into account curvature information and fit better the small-scale structures of the surface. 3) We penalize deviations of the tangent space to improve the appearance of sharp creases.

Computer Vision, on the other hand, has focused on developing energy models to fit subdivision surfaces to noisy data [30, 5, 12, 13], but has ignored the impact of outliers and the optimization on the accuracy of the surface. [12] fits a subdivision surface to range data by solving a weighted least-squares problem that assumes optimal correspondences between input point and domain parameters. This assumption is removed in [30, 5, 13] by explicitly optimizing the correspondences with least-squares models that preprocess the data to eliminate outliers and can only handle gross outliers. These methods also assume the topology of the surface to be known and initialize it with a manually-designed control mesh [30, 5] or a sphere [13]. The sphere initialization is flexible but over-smooths the surface because it prevents self intersections as the surface evolves. In terms of optimization, all these techniques use a Levenberg-Marquardt (LM) algorithm that estimates jointly the vertices of the control mesh and the correspondences between the input points and surface samples. This increases the size of the problem and slows the optimization because gradient-based techniques, like LM, only update the surface correspondences to adjacent faces of the control mesh. Our majorize-minimize (MM)

algorithm places no limits on these updates and can jump to different valleys of the energy landscape.

Our application of subdivision surfaces to shape analysis builds on the work of [14, 3, 33, 10] that investigate the accuracy of computing mass and stiffness matrices on a subdivision surface, but do not consider the estimation of wave-kernel signatures, geodesics, or shape matches in the subdivision framework.

7 Experiments

Experiments on Surface Compression

Our experiments compare our subdivision representation to triangular meshes with two different settings: reconstructing a surface from noisy Kinect pointclouds, and approximating a fine artifact-free mesh with small-scale structures. For all our experiments we set $q = 1.3$ and manually choose α, β to fit each shape and model (either our model or the state-of-the-art methods we compare to). When the input is a mesh, we set these parameters to minimize the Hausdorff distance between the subdivision surface and the input mesh.

Figures 1, 4 show that our subdivision surface reconstructs a surface from a noisy pointcloud as accurately as the mesh obtained by the state-of-the-art reconstruction technique [15] but reduces the number of representation variables to 2% of the mesh size. Our subdivision surfaces preserve the smooth regions and sharp corners (torso and hands of Figure 4), and texture details (human hair in Figure 1) of the fine mesh that are lost in a triangular mesh of the same size obtained by quadratic edge collapse.

For all our experiments with meshes, we use the high-resolution versions of the TOSCA dataset and fitted a subdivision surface with 1700 and 1000 vertices. Tables 1–2 report the execution time and the Hausdorff distance between the input mesh and our compressed subdivision representation for 72 high-resolution TOSCA meshes. Figures 5–7 show the subdivision surfaces fitted to the input meshes with the different models for a qualitative comparison.

Comparison to State-of-the-Art Models When the input is a noisy pointcloud, our surfaces avoid the artifacts of [23] because our energy model is robust to outliers (Figure 4). Robustness also guards us against erroneous corre-

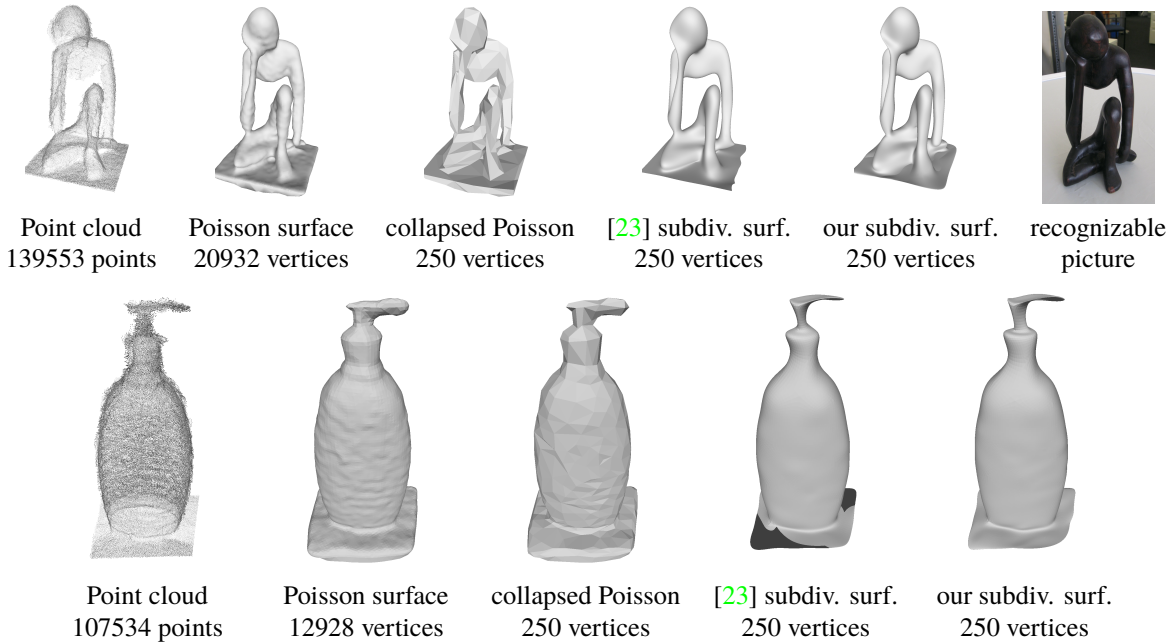


Figure 4: Surfaces reconstructed from a Kinect point cloud (columns 1) with a state of the art Poisson surface reconstruction method [15] (column 2) and with the proposed subdivision surface (columns 5). Our technique reconstructs and represents the surface with an accuracy comparable to a high-resolution mesh while compressing the representation to less than 2%. We reconstruct the nozzle of the bottle with higher accuracy thanks to our robust emery model. The subdivision surface of [23] (columns 4) shrinks the statue’s V-shaped torso while it oversmooths its hands and produces artifacts at the base of the bottle where samples are irregularly spaced and overlap.

spendences in thin structures of clean meshes. We also fit better small curved structures because we use a second-order distance approximation, instead of the first-order of [23], that takes into account curvature information. This is highlighted in the representation of mouths, eyes, and ears of Figures 5–7.

Comparison to State-of-the-Art Optimization We compare the subdivision surfaces obtained by optimizing our energy model with the proposed algorithm and by employing Levenberg-Marquardt to minimize the MM majorizer with respect to the mesh vertices and the correspondence parameters. Our optimization is an order of magnitude faster and less sensitive to local minima than the LM approach proposed by [30, 5, 12, 13]. As a result, our surfaces evolve further away from their initialization to reproduce the small-scale details of the input meshes (ears and mouths of Figure 5).

Our fitting technique is moderately slower than the quadratic model of [23] as a result of our robust energy, as expected. This speed loss is compensated by our improved surface quality, see Table 1.

Effects of the different terms in our energy model: Our model always benefits from the robust term while the tangent-fit is slightly detrimental in rare cases, see columns 1–3 in Table 1.

Experiments on Shape Analysis

Figure 3 compares the wave kernel signature [1] at a surface point w_x with three different discretizations: a fine triangular mesh, a coarse triangular mesh, and our subdivision surface. This signature is a shape descriptor that assigns to each point $x \in S$ a function w_x that depends on the value of the Δ -eigenfunctions and their eigenvalues

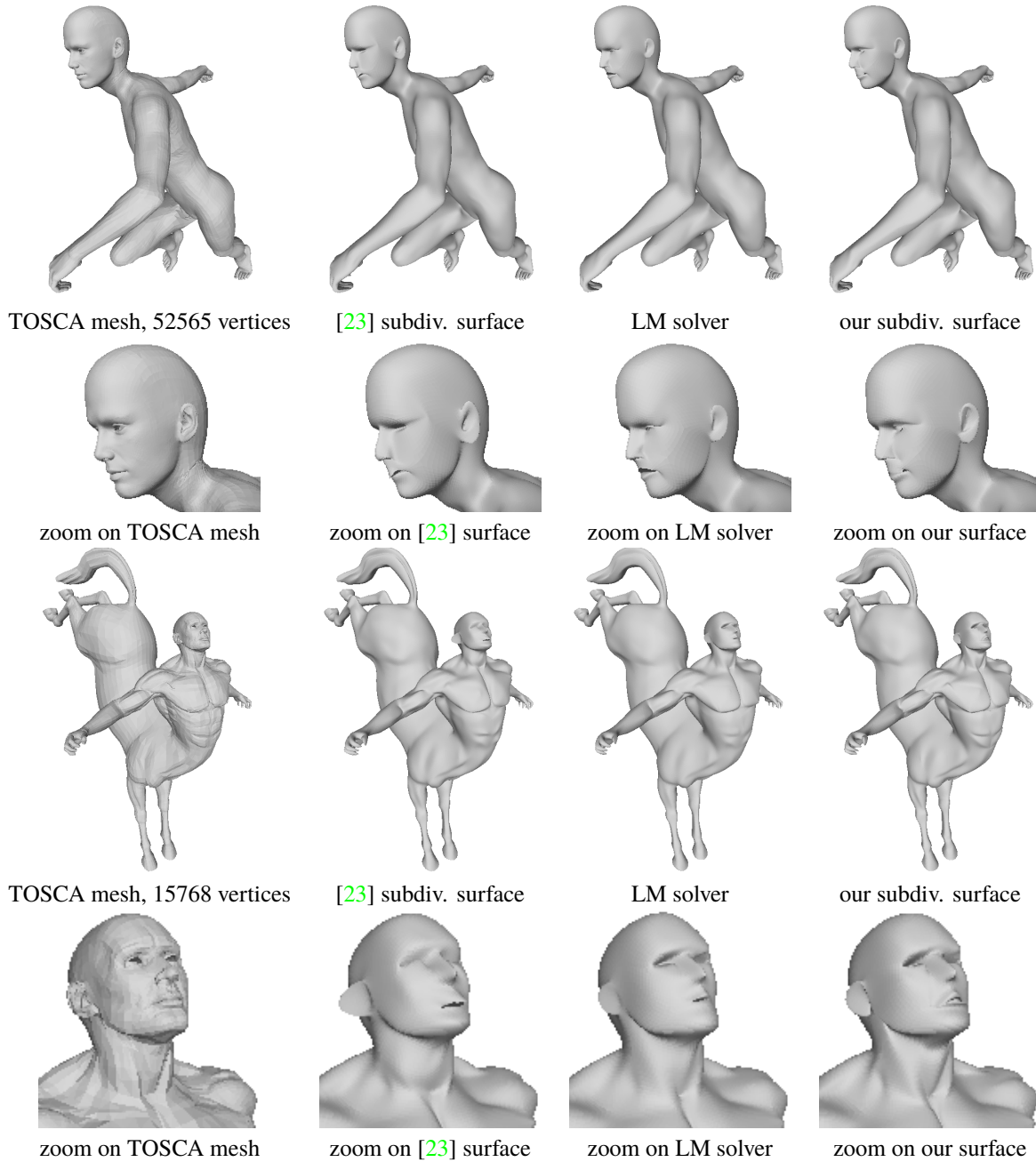


Figure 5: Comparison to state-of-the-art: high-resolution input mesh (column 1) mesh and subdivision surfaces fitted with [23] (column 2) and our proposed model optimized with Levenberg-Marquard (column 3) and our proposed optimization algorithm (column 4). Comparing columns 2 and 4, shows the benefits of using a robust q -power distance function and a second-order, instead of a first-order, approximation of the squared distance to the surface to fit thin surface structures like the ears or lips. Comparing columns 3 and 4 show the benefits of quadratic sequential program to avoid small-scale local minima close to the initialization that do not capture the shape details of the nose, lips, or mesh ears. All the subdivision surfaces have 1700 control vertices and are visualized by refining \mathbf{M}_0 3 times.

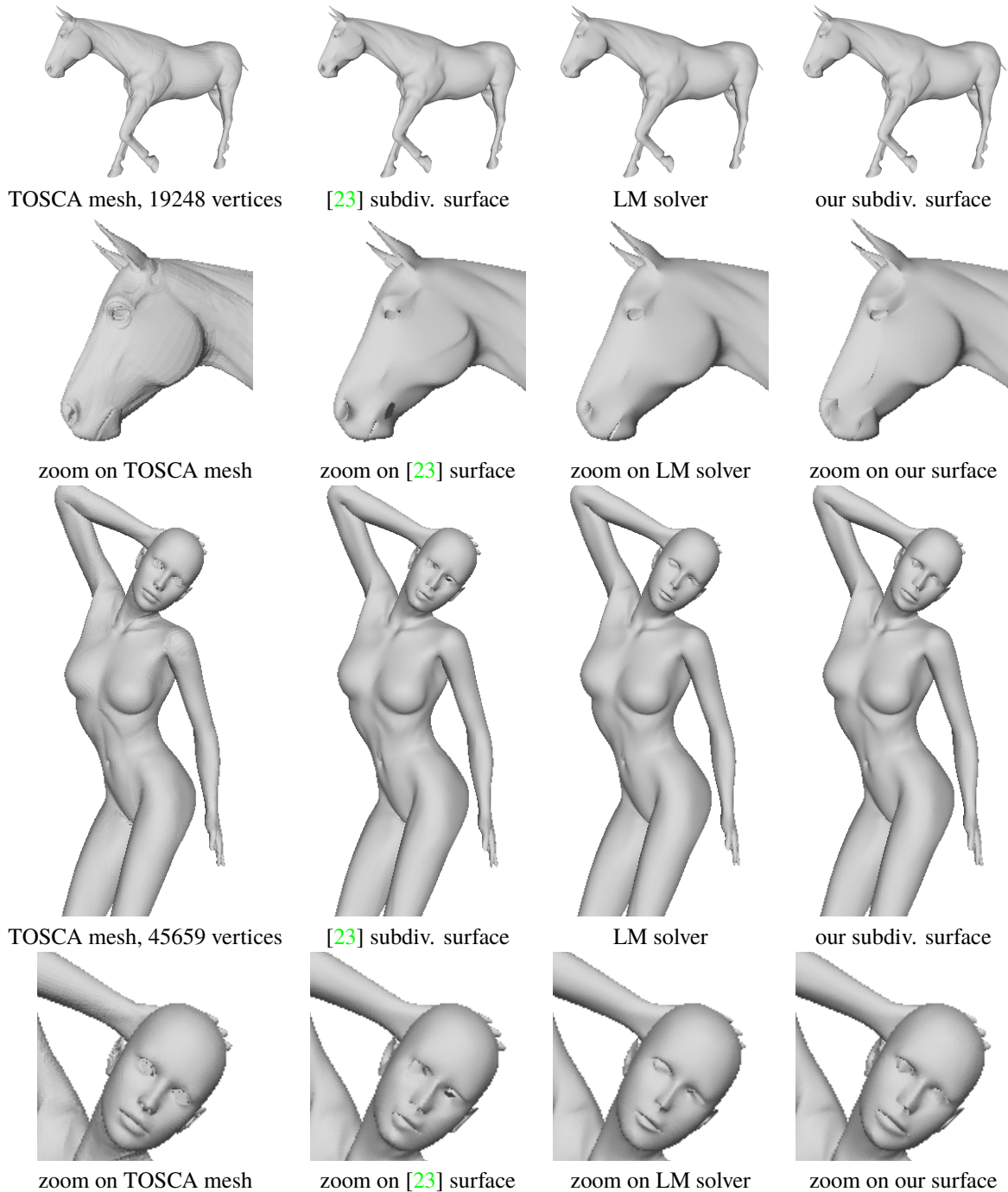


Figure 6: Comparison to state-of-the-art: high-resolution input mesh (column 1) mesh and subdivision surfaces fitted with [23] (column 2) and our proposed model optimized with Levenberg-Marquard (column 3) and our proposed optimization algorithm (column 4). Comparing columns 2 and 4, shows the benefits of using a robust q -power distance function to fit thin surface structures like the lips or mesh eyelids without artifacts. Comparing columns 3 and 4 show the benefits of quadratic sequential program to avoid small-scale local minima close to the initialization that do not capture the shape details of the nose, lips, or mesh ears. All the subdivision surfaces have 1700 control vertices and are visualized by refining M_0 3 times.

Table 1: Hausdorff distance (as a % of the bounding box diagonal) between the input mesh and a subdivision surface with 1000 and 1700 control vertices. Columns 1–3 and 6–8 show the importance of each term in the energy model, while columns 4–5 and 9–10 compare our algorithm to state-of-the-art model of [23] and to the Levenberg-Marquardt (LM) optimization advocated by [30, 5, 13].

mesh	1000 control vertices					1700 control vertices				
	$q = 2$	$\alpha = 0$	full model	[23]	LM solver	$q = 2$	$\alpha = 0$	full model	[23]	LM solver
cat0	0.180	0.176	0.158	0.209	0.237	0.113	0.103	0.103	0.123	0.141
cat1	0.251	0.237	0.218	0.295	0.327	0.160	0.155	0.148	0.192	0.192
cat10	0.213	0.201	0.019	0.246	0.251	0.132	0.123	0.121	0.155	0.184
cat2	0.436	0.390	0.352	0.475	0.572	0.272	0.256	0.240	0.300	0.366
cat3	0.210	0.200	0.183	0.259	0.263	0.128	0.127	0.126	0.155	0.165
cat4	0.254	0.247	0.232	0.303	0.345	0.168	0.166	0.154	0.195	0.209
cat5	0.219	0.208	0.201	0.254	0.286	0.139	0.131	0.129	0.166	0.165
cat6	0.390	0.390	0.359	0.454	0.443	0.260	0.257	0.240	0.313	0.313
cat7	0.437	0.391	0.373	0.468	0.483	0.268	0.253	0.246	0.304	0.444
cat8	0.233	0.209	0.197	0.251	0.261	0.156	0.145	0.139	0.168	0.189
cat9	0.283	0.263	0.248	0.336	0.356	0.179	0.171	0.166	0.204	0.238
centaur0	0.448	0.432	0.400	0.490	0.589	0.305	0.303	0.285	0.347	0.357
centaur1	0.508	0.449	0.424	0.507	0.526	0.323	0.321	0.298	0.361	0.374
centaur2	0.632	0.578	0.553	0.653	0.733	0.402	0.403	0.381	0.459	0.571
centaur3	0.443	0.446	0.417	0.489	0.597	0.306	0.310	0.289	0.352	0.361
centaur4	0.545	0.488	0.478	0.550	0.651	0.336	0.346	0.320	0.393	0.394
centaur5	0.474	0.466	0.441	0.521	0.563	0.319	0.325	0.304	0.371	0.422
david0	0.274	0.250	0.232	0.273	0.402	0.174	0.171	0.163	0.187	0.203
david1	0.403	0.377	0.370	0.445	0.645	0.275	0.262	0.255	0.296	0.502
david10	0.396	0.329	0.324	0.378	0.453	0.218	0.216	0.199	0.251	0.283
david11	0.477	0.434	0.421	0.479	1.004	0.313	0.293	0.284	0.351	0.410
david12	0.409	0.363	0.360	0.391	0.465	0.257	0.233	0.219	0.272	0.381
david13	0.349	0.341	0.321	0.381	0.647	0.238	0.227	0.216	0.253	0.304
david6	0.297	0.295	0.272	0.333	0.343	0.185	0.186	0.177	0.211	0.288
dog0	0.302	0.291	0.272	0.349	0.424	0.195	0.184	0.180	0.225	0.286
dog1	0.433	0.407	0.398	0.470	0.624	0.269	0.264	0.250	0.323	0.381
dog10	0.440	0.378	0.369	0.469	0.539	0.244	0.246	0.232	0.289	0.295
dog2	0.360	0.333	0.311	0.425	0.421	0.214	0.207	0.202	0.249	0.303
dog3	0.384	0.377	0.362	0.453	0.463	0.273	0.253	0.242	0.297	0.402
dog5	0.336	0.327	0.309	0.391	0.449	0.209	0.205	0.193	0.244	0.266
dog6	0.365	0.335	0.328	0.408	0.455	0.221	0.206	0.206	0.247	0.391
dog7	0.444	0.429	0.413	0.496	0.628	0.288	0.280	0.268	0.331	0.389
dog8	0.458	0.435	0.408	0.523	0.598	0.288	0.287	0.279	0.340	0.362
gorilla1	0.497	0.379	0.398	0.457	0.753	0.340	0.274	0.274	0.312	0.449
gorilla14	0.854	0.688	0.719	0.885	1.348	0.599	0.486	0.489	0.572	0.776
gorilla5	0.711	0.568	0.546	0.689	0.880	0.446	0.380	0.383	0.444	0.706
gorilla8	0.793	0.650	0.621	0.775	1.080	0.530	0.449	0.451	0.538	0.863
horse0	0.372	0.366	0.355	0.431	1.252	0.250	0.246	0.233	0.290	0.317
horse10	0.351	0.323	0.315	0.375	1.223	0.226	0.225	0.216	0.274	0.294
horse14	0.370	0.348	0.343	0.422	0.457	0.246	0.248	0.240	0.298	0.346
horse15	0.352	0.331	0.336	0.399	0.478	0.230	0.230	0.212	0.273	0.281
horse17	0.379	0.356	0.352	0.414	0.448	0.257	0.250	0.239	0.297	0.342
horse5	0.416	0.374	0.364	0.430	0.484	0.260	0.264	0.250	0.314	0.370
horse6	0.353	0.350	0.340	0.411	0.424	0.233	0.237	0.222	0.283	0.309
horse7	0.351	0.333	0.327	0.398	0.435	0.238	0.233	0.224	0.284	0.284
michael0	0.309	0.276	0.266	0.320	0.392	0.185	0.189	0.176	0.210	0.257
michael1	0.376	0.340	0.333	0.396	0.480	0.246	0.226	0.214	0.256	0.322
michael10	0.417	0.373	0.346	0.418	0.618	0.267	0.256	0.240	0.290	0.384
michael11	0.665	0.576	0.547	0.681	0.879	0.443	0.409	0.412	0.475	0.904
michael12	0.436	0.365	0.344	0.431	0.507	0.268	0.262	0.255	0.297	0.394
michael13	0.438	0.371	0.364	0.422	0.698	0.283	0.267	0.255	0.296	0.382
michael15	0.440	0.387	0.369	0.449	0.639	0.283	0.263	0.258	0.294	0.427
michael16	0.403	0.366	0.349	0.416	0.552	0.263	0.259	0.249	0.296	0.459
michael18	0.431	0.371	0.346	0.422	0.594	0.266	0.255	0.245	0.285	0.449
michael19	0.417	0.381	0.367	0.433	0.517	0.259	0.254	0.243	0.294	0.363
michael2	0.578	0.476	0.470	0.537	0.647	0.358	0.325	0.318	0.365	0.527
michael3	0.426	0.356	0.346	0.413	0.564	0.262	0.249	0.233	0.279	0.278
michael4	0.414	0.364	0.350	0.415	0.600	0.264	0.249	0.239	0.282	0.386
michael5	0.366	0.326	0.313	0.384	0.454	0.222	0.220	0.206	0.251	0.342
michael6	0.384	0.363	0.349	0.411	0.453	0.248	0.234	0.227	0.265	0.325
michael7	0.474	0.394	0.365	0.450	0.645	0.287	0.273	0.258	0.311	0.387
victoria1	0.321	0.267	0.281	0.330	0.365	0.194	0.176	0.166	0.205	0.298
victoria10	0.278	0.275	0.252	0.314	0.567	0.165	0.166	0.156	0.202	0.239
victoria17	0.370	0.305	0.309	0.357	0.436	0.203	0.190	0.174	0.222	0.310
victoria2	0.302	0.267	0.243	0.322	0.363	0.164	0.157	0.150	0.189	0.240
victoria21	0.537	0.449	0.457	0.532	1.168	0.322	0.293	0.281	0.337	0.449
victoria24	0.311	0.293	0.277	0.354	0.416	0.188	0.173	0.169	0.205	0.329
victoria25	0.283	0.258	0.233	0.312	0.377	0.152	0.144	0.137	0.174	0.236
victoria4	0.296	0.280	0.267	0.317	0.390	0.174	0.167	0.160	0.197	0.243
wolf0	0.429	0.427	0.414	0.477	0.510	0.331	0.334	0.320	0.355	0.431
wolf1	0.410	0.419	0.389	0.455	0.517	0.298	0.315	0.293	0.335	0.367
wolf2	0.443	0.463	0.427	0.501	0.570	0.330	0.345	0.327	0.363	0.471

Table 2: Execution time (in seconds) to fit a subdivision surface with 1000 and 1700 control vertices. Columns 1–3 and 6–8 show how each additional term in the energy model slows the optimization, while columns 4–5 and 9–10 compare our technique to state-of-the-art model of [23] and to the Levenberg-Marquardt (LM) optimization algorithm advocated by [30, 5, 13].

mesh	1000 control vertices					1700 control vertices				
	$q = 2$	$\alpha = 0$	full model	[23]	LM solver	$q = 2$	$\alpha = 0$	full model	[23]	LM solver
cat0	32.7	34.7	56.0	20.8	408.0	24.6	44.5	36.0	18.6	346.5
cat1	37.1	41.2	44.0	12.9	345.2	34.5	43.3	52.6	15.1	367.5
cat10	24.7	36.5	34.9	18.2	403.3	30.3	50.0	38.7	37.4	544.6
cat2	23.5	33.9	43.6	21.3	450.0	31.3	44.3	42.3	21.0	399.9
cat3	28.1	36.6	47.4	16.4	333.7	41.5	51.8	32.4	18.6	382.5
cat4	30.6	43.4	46.7	16.5	344.1	28.6	34.8	54.7	20.6	384.0
cat5	18.7	38.8	41.6	17.4	547.1	29.6	47.3	33.4	17.1	372.9
cat6	24.9	43.9	40.7	18.0	365.1	28.5	48.3	41.1	16.1	332.3
cat7	30.1	23.9	40.9	14.3	402.6	26.6	50.9	51.4	20.3	468.0
cat8	34.7	42.1	35.9	17.4	267.5	27.4	48.7	44.1	20.8	378.9
cat9	22.6	35.7	56.6	19.1	361.4	35.5	29.7	47.2	17.0	468.4
centaur0	20.7	16.5	21.5	8.2	165.4	16.2	22.1	24.0	15.8	185.1
centaur1	12.0	21.9	16.5	8.9	279.3	23.8	22.0	33.7	11.7	374.1
centaur2	16.0	15.9	26.0	9.9	209.2	19.2	24.9	24.1	10.4	171.3
centaur3	18.3	14.1	25.9	8.5	192.4	18.8	21.9	26.4	10.2	258.7
centaur4	16.9	24.0	26.9	8.8	267.1	24.2	28.3	27.9	11.3	307.5
centaur5	14.3	17.0	28.1	8.8	254.2	18.9	25.0	25.9	9.8	197.1
david0	59.5	59.4	86.9	39.3	602.6	64.8	56.1	63.4	40.2	473.5
david1	58.8	56.4	70.1	34.9	447.5	60.1	55.2	63.0	36.0	799.9
david10	44.7	47.1	72.1	37.6	589.8	59.0	59.8	79.9	40.2	611.4
david11	68.1	58.2	128.5	37.3	683.6	59.2	76.5	100.4	33.1	713.5
david12	63.4	52.0	61.7	38.8	528.8	63.8	53.2	74.9	45.6	622.2
david13	61.0	45.7	86.8	37.4	807.0	58.8	58.4	108.8	43.0	832.3
david6	50.9	42.6	71.3	30.7	592.7	54.2	60.7	63.2	33.7	551.9
dog0	20.7	25.4	48.8	14.0	325.0	23.2	31.1	39.6	14.6	321.8
dog1	22.9	27.4	30.1	15.7	281.2	39.2	39.6	41.8	16.8	368.4
dog10	21.4	30.5	39.6	12.8	283.4	31.0	31.4	32.8	15.0	348.5
dog2	28.1	27.2	38.9	14.3	251.6	29.3	45.7	48.0	18.8	323.8
dog3	21.1	34.0	32.3	16.1	303.0	28.3	27.1	34.1	15.4	311.2
dog5	31.7	28.2	44.8	20.4	271.4	34.3	48.8	34.8	17.5	207.0
dog6	35.4	31.3	53.0	18.8	293.2	24.8	45.5	49.4	18.5	378.7
dog7	21.0	28.3	38.6	15.2	427.1	44.0	47.4	45.0	22.2	355.7
dog8	20.4	27.4	41.8	14.8	304.5	28.5	45.4	37.6	15.7	366.5
gorilla1	36.8	33.0	61.2	23.6	531.9	45.8	48.3	64.4	34.1	416.0
gorilla14	32.8	41.3	52.9	21.0	519.9	41.6	72.1	65.6	25.3	620.7
gorilla5	37.9	47.2	55.1	38.3	565.8	28.3	55.3	63.8	24.3	837.3
gorilla8	46.5	44.5	59.6	19.9	436.8	37.8	64.6	69.5	26.9	695.7
horse0	29.6	22.5	46.4	12.9	98.6	22.0	42.0	34.0	13.0	234.2
horse10	23.1	26.7	47.0	12.6	120.0	34.9	36.7	32.1	11.8	302.6
horse14	17.5	26.2	31.8	13.4	261.4	30.9	45.8	45.9	13.2	406.2
horse15	17.5	21.6	34.1	12.0	489.1	20.1	24.3	40.4	16.5	252.8
horse17	16.9	22.6	21.4	13.9	233.1	24.9	35.5	36.8	13.1	316.4
horse5	17.2	28.9	30.5	13.2	322.4	29.3	35.0	37.5	16.5	346.2
horse6	23.2	34.8	25.4	11.2	250.3	30.2	44.5	38.8	13.1	254.3
horse7	28.0	24.0	38.6	11.1	194.6	19.7	29.8	28.0	12.7	290.6
michael0	63.1	54.9	74.1	37.4	632.1	60.2	54.9	76.2	40.9	599.8
michael1	64.5	55.0	86.9	47.2	588.5	56.3	56.5	63.7	44.5	909.7
michael10	54.4	63.1	108.5	38.4	476.4	69.4	51.8	76.5	29.3	517.2
michael11	44.1	80.9	115.8	29.3	583.0	54.3	56.9	84.3	31.3	762.0
michael12	79.7	75.2	100.4	37.2	607.9	77.8	61.6	118.6	40.5	573.2
michael13	53.7	70.3	103.5	39.0	553.5	52.2	51.5	71.6	39.4	546.4
michael15	66.4	61.5	121.4	34.5	690.1	62.5	53.3	68.3	38.2	443.0
michael16	46.8	50.9	65.4	47.8	495.6	80.9	69.7	72.0	56.1	571.5
michael18	59.0	60.1	98.9	32.9	311.1	55.9	69.6	78.6	34.9	472.5
michael19	53.6	52.5	58.6	34.6	473.3	71.0	65.9	60.5	38.0	535.3
michael2	55.3	54.4	55.5	35.4	764.9	61.2	47.2	68.9	35.7	476.2
michael3	51.8	57.4	95.9	36.2	452.0	52.8	49.6	60.7	38.3	658.7
michael4	48.6	47.5	76.3	33.7	569.7	76.4	52.2	70.8	36.3	576.4
michael5	77.6	59.3	106.4	27.4	468.1	57.1	53.4	57.7	38.9	1117.8
michael6	63.6	39.5	68.5	26.5	389.0	68.5	67.0	65.8	37.6	439.6
michael7	55.4	65.5	96.4	35.0	508.0	62.0	57.8	62.4	40.5	489.5
victoria1	49.7	49.4	52.5	29.3	439.4	30.3	38.9	52.5	27.5	381.9
victoria10	41.8	36.8	40.3	24.4	527.8	59.3	60.4	57.3	30.3	405.8
victoria17	39.2	64.7	55.6	27.7	582.8	45.0	43.9	72.0	30.6	534.7
victoria2	53.5	38.0	45.8	27.6	448.4	48.0	57.0	67.9	27.6	584.8
victoria21	35.1	69.0	80.2	27.0	321.3	37.5	42.9	68.9	24.5	444.0
victoria24	40.7	46.2	84.5	22.7	366.5	27.6	47.2	76.1	26.8	549.3
victoria25	49.9	52.9	57.7	23.6	308.4	47.3	79.1	65.5	28.5	412.3
victoria4	46.5	43.7	60.4	27.5	393.3	41.6	46.4	58.7	23.7	478.4
wolf0	7.4	12.1	11.5	6.8	64.2	10.6	16.7	9.1	5.7	114.0
wolf1	6.5	8.5	9.1	8.2	78.5	17.0	22.8	15.8	16.6	137.9
wolf2	7.0	8.0	9.7	5.7	52.9	8.0	11.6	16.7	8.1	106.7

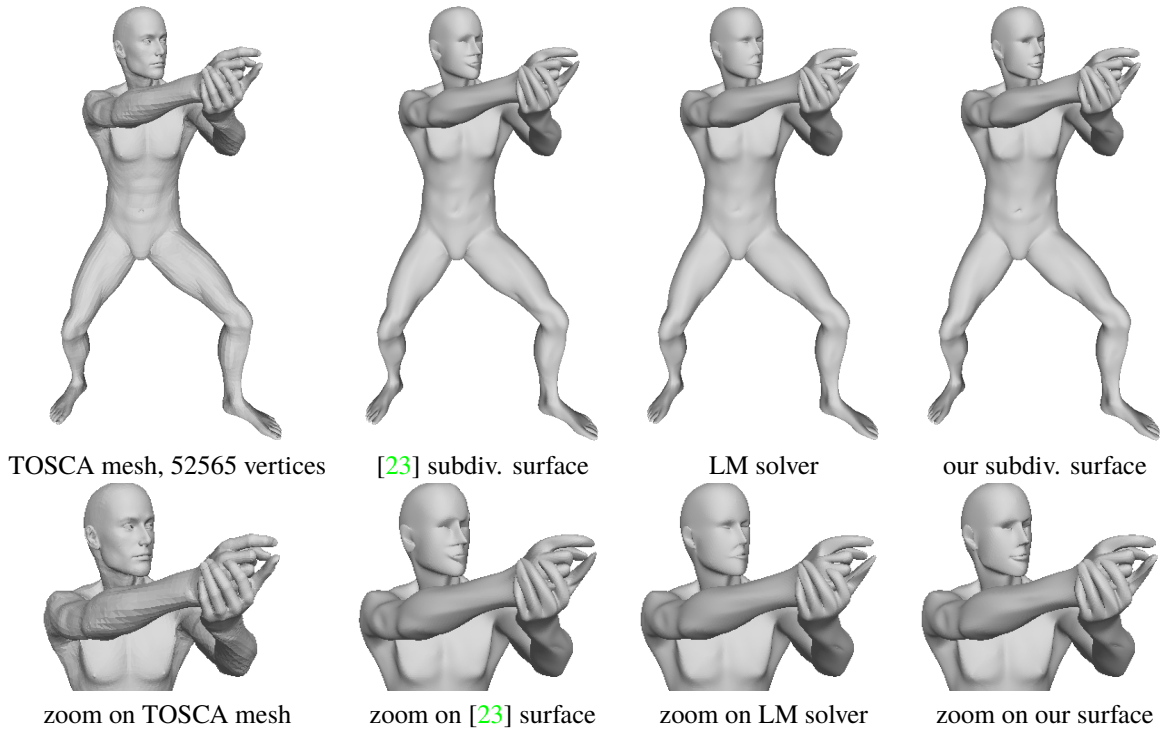


Figure 7: Comparison to state-of-the-art: high-resolution input mesh (column 1) mesh and subdivision surfaces fitted with [23] (column 2) and our proposed model optimized with Levenberg-Marquard (column 3) and our proposed optimization algorithm (column 4). Comparing columns 2 and 4, shows the benefits of using the second-order, instead of a first-order, approximation of the squared distance to the surface to capture the curvature details of small structures like the mesh ears. Comparing columns 3 and 4 show the benefits of quadratic sequential program to avoid small-scale local minima close to the initialization that do not capture the shape details of the nose, lips, or mesh eyes. All the subdivision surfaces have 1700 control vertices and are visualized by refining M_0 3 times.

at x . The point signature of coarse mesh is different from the signature of fine mesh, which is well matched by the subdivision surface.

The functional map framework [25] formulates the problem of matching points of two shapes as matching smooth functions over them. The problem is invariant to isometric transformations by representing smooth function with Δ -eigenfunctions and by finding a linear map between these eigenfunctions. Figure 8 shows the computed matching with respect to two different shape representations: a fine mesh with 27894 vertices and a subdivision surface with 1700 control vertices. Our experiments show comparable matching results with a slight loss of accu-

racy at the tails of some cats, but this is compensated by a surface representation and matching problem of 10% of the original size. To visualize the results, we show a template shape with a color map that interprets the three spatial coordinates of every point as RGB color information and transfer this color map to each target shape with the matching estimated with functional maps [25]. In this experiment, using a coarse triangular mesh to do the shape matching simply fails.

Figures 1–10 compare geodesics computed by the Heat method [7] with different surface representations fitted to the Kinect pointclouds of Figures 1 and 4. As a proxy for ground-truth, we use a high-resolution triangular mesh

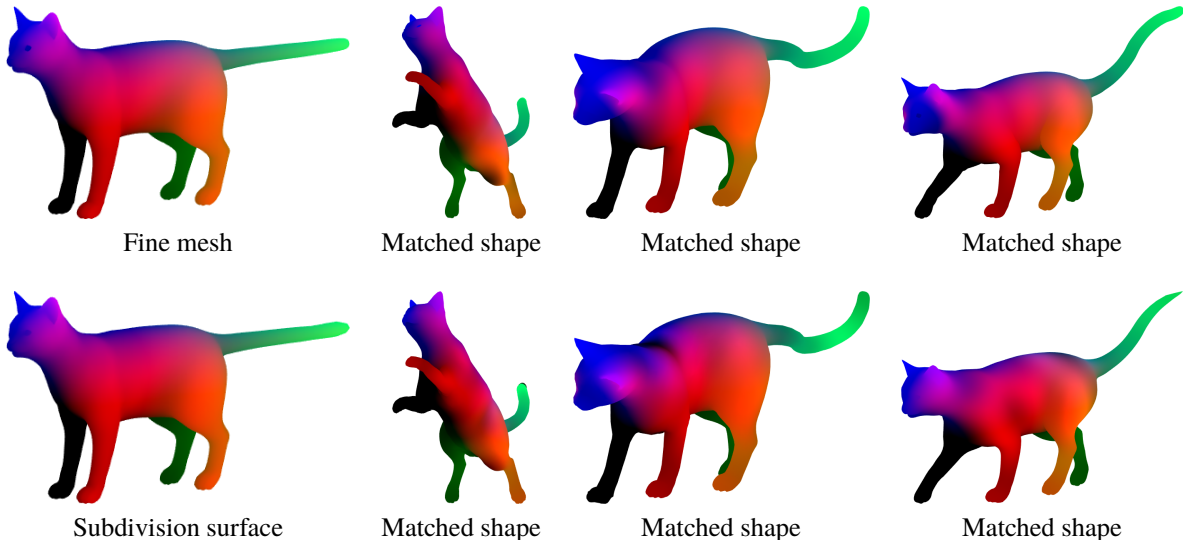


Figure 8: Shape matching results of the functional map framework [25]. After the matching is determined, the color information of the target shape is transferred to the matched shape with the mapping estimated by functional maps[25].

obtained by the Poisson reconstruction method [15] and compare it to two compressed surface representations of the same size: a low-resolution triangular mesh obtained by quadratic edge collapse [9] of the high-resolution mesh and our subdivision representation. Our subdivision surface is comparable to the high-resolution mesh and can be used to compress both the shape and its geodesics functions. In contrast, the low-resolution triangular mesh provides a discretization too coarse to represent the small scale details of the surface and its geodesic. To highlight the loss of small-scale structure on the geodesic, we represent the level lines of the geodesic at high and low resolution and demonstrate how the geodesic estimated from the coarse triangular mesh is unable to capture the high-frequency information of the geodesic (as estimated from the high-resolution mesh) while our surface representation captures both low and high frequency information accurately.

8 Conclusions

We have presented a method to compress surfaces with a representation well suited for shape analysis. To this purpose, we fit a subdivision surface to low-level surface

representations and develop standard shape analysis operators with it.

Our surface fitting model is robust to noise and outliers and can handle both clean input meshes and noisy point cloud obtained from real data. The resulting subdivision surfaces let us represent smooth shapes at high accuracy with a fraction of the variables used in triangular meshes and use the same subdivision schemes to parametrize functions over the surface and compute tangent spaces or curvatures analytically. Our experiments show how the smoothness of the representation reduces the size of the Laplace-Beltrami operator and its eigenfunctions without loss of accuracy and allows us to compute wave-kernel signatures, approximate geodesics, and shape matches in a compact representation.

A Appendix: Quadratic Solver

We optimize the objective energy

$$\min_S E(S) = \underbrace{\text{dist}(S, \mathbf{P})}_{\text{Point Fit}} + \underbrace{\alpha \mathcal{T}(S, \mathbf{T})}_{\text{Tangent Fit}} + \underbrace{\beta R(S)}_{\text{Regularization}}, \quad (9)$$

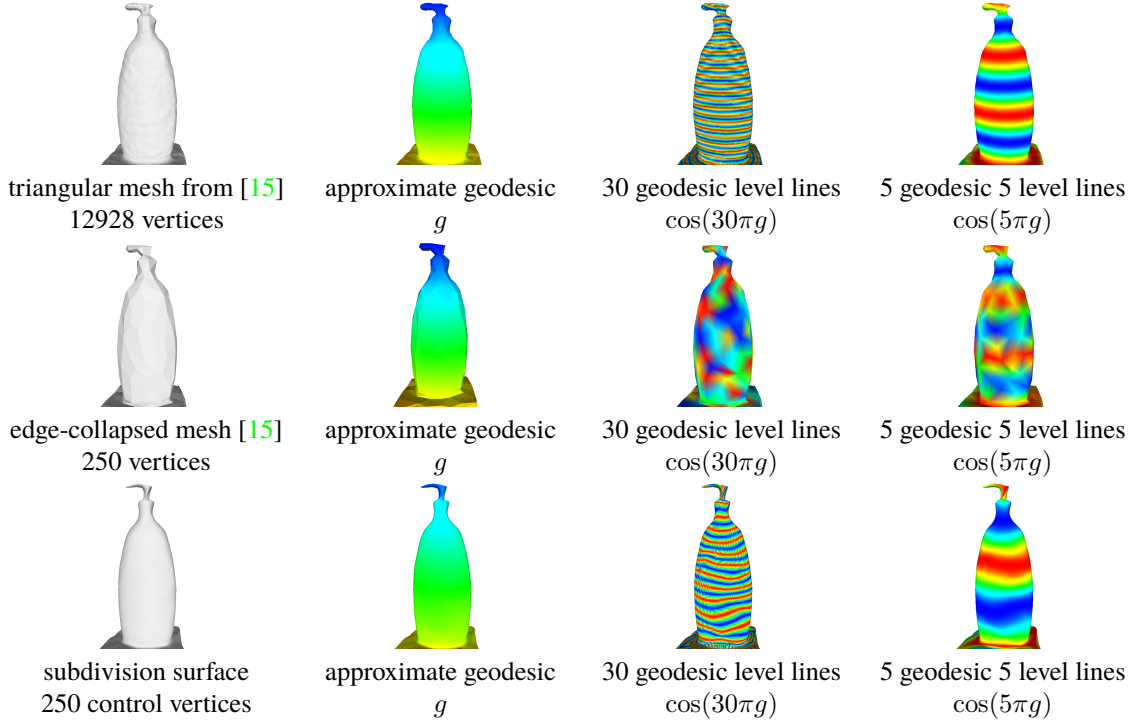


Figure 9: Computation of approximate geodesics by the Heat method [7] with different surface representations fitted to a Kinect pointcloud. Column 1: representation of the surface with a high-resolution mesh obtained with Poisson reconstruction [15] (row 1), a low-resolution triangular mesh obtained by edge collapse of the high-resolution mesh (row 2), and with our subdivision surface (row 3). Column 2: approximate geodesic g estimated with the Heat method [7] on each surface representation. Columns 3 and 4: level lines of the geodesics visualized as $\cos(\varpi g)$, with $\varpi = 30\pi$ in column 3 and $\varpi = 5\pi$ in column 4. Our subdivision surface is comparable to the surface obtained with the Poisson reconstruction method [15] and can faithfully represent geodesics at both low and high resolution even though it has 2% of its vertices. In contrast, compressing the state-of-the-art mesh with the quadratic edge collapse method of [9] loses all the small scale details of the surface and its geodesics. This is highlighted by representing the level lines of the geodesic on the mesh at high resolution (column 3) where we show how the discretization associated with a coarse triangular mesh representation cannot estimate the high-frequency information of the geodesic accurately.

that fits a subdivision surface S to a set of point \mathbf{P} and normal data \mathbf{T} by solving a sequence of convex problems

$$V^{m+1} \leftarrow \min_V V^\top (Q^m V - b^m) \quad (10)$$

over the vertices $V = [v_1, \dots, v_n]$ of the control mesh \mathbf{M} . In this section, we show how to obtain the quadratic objective function $V^\top (Q^m V - b^m)$ that approximates the original energy at iteration m .

Following a majorize-minimize (MM) principle, at it-

eration m we substitute our robust energy by the weighted least-squares problem

$$\min_{U, V} \sum_{j=1}^N w_j^m \|p_j - \Phi(u_j)\|^2 + \sum_{i=1}^2 \alpha_{ij}^m \langle t_j, \partial_i \Phi(u_j) \rangle^2 + \beta \|RV\|^2 \quad (11)$$

over the mesh vertices V and the correspondence parameters $u_1, \dots, u_N \in \mathcal{T}_{\mathbf{M}}$. The parametrization of the sub-

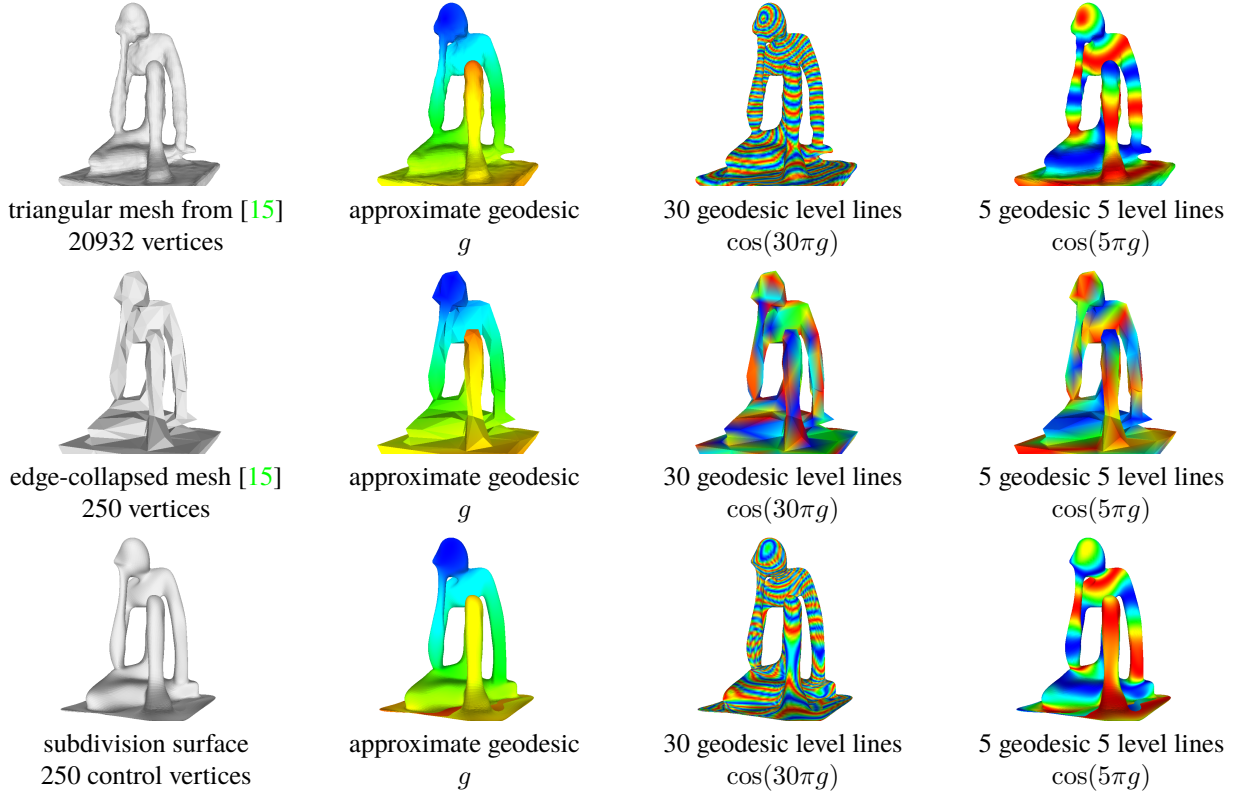


Figure 10: Computation of approximate geodesics by the Heat method [7] with different surface representations fitted to a Kinect pointcloud. Column 1: representation of the surface with a high-resolution mesh obtained with Poisson reconstruction [15] (row 1), a low-resolution triangular mesh obtained by edge collapse of the high-resolution mesh (row 2), and with our subdivision surface (row 3). Column 2: approximate geodesic g estimated with the Heat method [7] on each surface representation. Columns 3 and 4: level lines of the geodesics visualized as $\cos(\varpi g)$, with $\varpi = 30\pi$ in column 3 and $\varpi = 5\pi$ in column 4. Our subdivision surface is comparable to the surface obtained with the Poisson reconstruction method [15] and can faithfully represent geodesics at both low and high resolution even though it has 2% of its vertices. In contrast, compressing the state-of-the-art mesh with the quadratic edge collapse method of [9] loses all the small scale details of the surface and its geodesics. This is highlighted by representing the level lines of the geodesic on the mesh at high resolution (column 3) where we show how the discretization associated with a coarse triangular mesh representation cannot estimate the high-frequency information of the geodesic accurately.

division surface

$\Phi_i(u_j)$ that samples the surface as

$$\Phi(u) = \sum_{i=1}^n v_i \Phi_i(u),$$

$$x_j = \sum_{i=1}^n v_i \Phi_i(u_j) \quad j = 1, \dots, N \quad X = L \cdot V.$$

depends linearly on the mesh vertices and can be described compactly with an $N \times n$ sparse matrix L with $L_{ji} =$

Analogously, we define L_1 and L_2 for the partial deriva-

tives of the basis functions

$$\partial_i \Phi(u_j) = \sum_{k=1}^n L_{i,jk} v_k \quad (12)$$

and introduce the auxiliary variables $x'_{ij} = \partial_i \Phi(u_j)$ that sample the tangent plane of the surface by

$$X'_i = L_i \cdot V \in \mathbb{R}^{N \times 3}.$$

We remove the variables u_j from the optimization by approximating the squared distance with the quadratic expression in V

$$\begin{aligned} \sum_{j=1}^n w_j^m \|p_j - \Phi(u_j)\|^2 &\approx \sum_{j=1}^n w_j^m \|p_j - (L \cdot V)_j\|_{D_j^m}^2, \\ &\approx \sum_{j=1}^n w_j^m (p_j - x_j)^\top D_j^m (p_j - x_j) \end{aligned}$$

where the symmetric positive definite matrix

$$D_j^m = \frac{d}{d + \rho_1} \tau_1 \tau_1^\top + \frac{d}{d + \rho_2} \tau_2 \tau_2^\top + \nu \nu^\top \quad (13)$$

is determined by the approximation to the squared distance to the surface S^m at p_j . In particular, x_j is a surface point close to p_j (but not necessarily its projection onto S^m), d is the distance from p_j to this point, and $\rho_1, \rho_2, \tau_1, \tau_2, \nu$ are the absolute values of the principal curvature radii, the principal curvature directions, and the normal to the surface S^m at x_j . Considering D_j^m independent of x_j at iteration m , the data fit term defines a quadratic problem.

The tangent fit energy

$$\sum_{j=1}^N \sum_{i=1}^2 \alpha_{ij}^m \langle t_j, \partial_i \Phi^m(u_j) \rangle^2 = \sum_{j=1}^N \sum_{i=1}^2 \alpha_{ij}^m \langle t_j, (L_i^m \cdot V)_j \rangle^2.$$

is also quadratic in V . Due to non-negative α_{ij}^m this expression is positive semi-definite. As the regularization $\|RV\|^2 = V^\top R^\top RV$ is also quadratic and positive semi-definite, we can efficiently solve the linear system that characterizes its unique minimum with the conjugate gradient method. This method is well suited to the problem at hand, because the matrices that define our quadratic objective are sparse and we can use the MM iterations to warm start the optimization at iteration m with the solution at iteration $m - 1$.

After optimizing V at iteration m , we update the parameter values u_1, \dots, u_n where we approximate the squared distance to the surface with the matrices D_1^m, \dots, D_n^m . In particular, we sample the surface $S^m = \Phi^m(\mathcal{T}_M)$ uniformly and create a kd-tree from these samples to find quickly the parameters $u_j \in \mathcal{T}_M$ of the surface sample closest to each input point $p_j \in \mathbf{P}$. Although this update strategy might seem reminiscent of coordinate descent, our combination of coordinate updates with the quadratic approximation corresponds to applying a quasi-Newton algorithm [32, 20] to the majorizer to avoid the slow convergence rates of coordinate descent. This removes the correspondence parameters from the optimization but can affect the majorizing property of (11) and puts our algorithm into the category of quadratic sequential programs instead of majorize-minimize algorithms. For this reason, we stop the process as soon as the original energy $E(\cdot)$ does not decrease any more. Our experiments indicate that this method provides better results than state-of-the-art methods.

References

- [1] M. Aubry, U. Schlickewei, and D. Cremers. The wave kernel signature: A quantum mechanical approach to shape analysis. In *IEEE ICCV*, pages 1626–1633, 2011. [1](#), [3](#), [10](#)
- [2] A. Bronstein, M. Bronstein, and R. Kimmel. *Numerical Geometry of Non-Rigid Shapes*. Springer, 2008. [1](#)
- [3] D. Burkhart, B. Hamann, and G. Umlauf. Iso-geometric finite element analysis based on Catmull-Clark subdivision solids. *Eurographics Symp. Geom. Process.*, 29(5):1575–1584, 2010. [9](#)
- [4] F. Calakli and G. Taubin. SSD: Smooth Signed Distance Surface Reconstruction. *Comput. Graph. Forum*, 30(7):1993–2002, sep 2011. [2](#)
- [5] T. J. Cashman and A. W. Fitzgibbon. What shape are dolphins? building 3D morphable models from 2D images. *IEEE Trans. Pattern Anal. Mach. Intell.*, 35(1):232–244, 2013. [6](#), [7](#), [9](#), [10](#), [13](#), [14](#)
- [6] E. Catmull and J. Clark. Recursively generated b-spline surfaces on arbitrary topological meshes. *Computer-Aided Design*, 10(6):350 – 355, 1978. [4](#)
- [7] K. Crane, C. Weischedel, and M. Wardetzky. Geodesics in heat: A new approach to computing distance based on heat flow. *ACM Trans. Graph.*, 32(3):10, 2013. [1](#), [2](#), [3](#), [8](#), [15](#), [17](#), [18](#)

- [8] V. Estellers, M. Scott, and S. Soatto. Robust Surface Reconstruction. *SIAM J. Imaging Sci.*, 9(4):2073–2098, jan 2016. [2](#)
- [9] M. Garland and P. S. Heckbert. Surface simplification using quadric error metrics. *SIGGRAPH*, pages 209–216, 1997. [2](#), [5](#), [16](#), [17](#), [18](#)
- [10] F. Goes, M. Desbrun, M. Meyer, and T. DeRose. Subdivision Exterior Calculus for Geometry Processing. *ACM Trans. Graph. Artic.*, 35(10), 2016. [9](#)
- [11] H. Hoppe, T. DeRose, T. Duchamp, M. Halstead, H. Jin, J. McDonald, J. Schweitzer, and W. Struetzle. Piecewise smooth surface reconstruction. *Comput. Graph. (ACM)*, pages 294–302, 1994. [9](#)
- [12] S. Ili. Using Subdivision Surfaces for 3D Reconstruction from Noisy Data. *Deform. Image Regist. Deform. Environ.*, pages 1—10, 2006. [6](#), [7](#), [9](#), [10](#)
- [13] M. Jaimez, T. J. Cashman, A. Fitzgibbon, J. Gonzalez-jimenez, and D. Cremers. An Efficient Background Term for 3D Reconstruction and Tracking with Smooth Surface Models. *IEEE Conf. Comput. Vis. Pattern Recognit.*, 2017. [2](#), [6](#), [7](#), [9](#), [10](#), [13](#), [14](#)
- [14] B. Jüttler, A. Mantzaflaris, R. Perl, and M. Rumpf. On numerical integration in isogeometric subdivision methods for {PDEs} on surfaces. *Computer Methods in Applied Mechanics and Engineering*, 302:131 – 146, 2016. [3](#), [9](#)
- [15] M. Kazhdan and H. Hoppe. Screened poisson surface reconstruction. *ACM Trans. Graph.*, 32(3):1–13, jun 2013. [2](#), [6](#), [9](#), [10](#), [15](#), [17](#), [18](#)
- [16] V. Kolmogorov. Blossom v: a new implementation of a minimum cost perfect matching algorithm. *Mathematical Programming Computation*, 1(1):43–67, July 2009. [6](#)
- [17] G. Lavoué, F. Dupont, and A. Baskurt. Subdivision surface fitting for efficient compression and coding of 3D models. *Vis. Commun. Image Process.*, 5960(33):59603F–59603F–12, 2005. [9](#)
- [18] B. Levy. Laplace-Beltrami Eigenfunctions: Towards an Algorithm that Understand s Geometry. *IEEE Int. Conf. Shape Model. Appl. inv ited talk*, 2006, 2006. [1](#)
- [19] R. Litman and A. M. Bronstein. Learning spectral descriptors for deformable shape correspondence. *IEEE Trans. Pattern Anal. Mach. Intell.*, 36(1):171–180, 2014. [1](#)
- [20] Y. Liu and W. Wang. A revisit to least squares orthogonal distance fitting of parametric curves and surfaces. *Lect. Notes Comput. Sci.*, 4975 LNCS(1):384–397, 2008. [6](#), [9](#), [19](#)
- [21] W. E. Lorensen and H. E. Cline. Marching cubes: A high resolution 3D surface construction algorithm. *ACM SIGGRAPH Comput. Graph.*, 21(4):163–169, 1987. [6](#)
- [22] W. Ma, X. Ma, S. K. Tso, and Z. Pan. Subdivision surface fitting from a dense triangle mesh. *Proc. - Geom. Model. Process. Theory Appl. GMP 2002*, 36:94–103, 2002. [9](#)
- [23] M. Marinov and L. Kobbelt. Optimization methods for scattered data approximation with subdivision surfaces. *Graph. Models*, 67(5):452–473, 2005. [9](#), [10](#), [11](#), [12](#), [13](#), [14](#), [15](#)
- [24] C. Notes and D. Zorin. Subdivision for Modeling and Animation. *New York*, 98:1 – 203, 2000. [1](#)
- [25] M. Ovsjanikov, M. Ben-Chen, J. Solomon, A. Butscher, and L. Guibas. Functional maps. *ACM Trans. Graph.*, 31(4):1–11, jul 2012. [1](#), [3](#), [15](#), [16](#)
- [26] H. Pottmann and S. Leopoldseder. A concept for parametric surface fitting which avoids the parametrization problem. *Comput. Aided Geom. Des.*, 20(6):343–362, 2003. [6](#), [9](#)
- [27] J. F. Remacle, J. Lambrechts, B. Seny, E. Marchandise, A. Johnen, and C. Geuzainet. Blossom-Quad: A non-uniform quadrilateral mesh generator using a minimum-cost perfect-matching algorithm. *Int. J. Numer. Methods Eng.*, 89(9):1102–1119, 2012. [5](#)
- [28] M. Reuter, F.-E. Wolter, and N. Peinecke. {Laplace-Beltrami} Spectra As 'Shape-{DNA}' of Surfaces and Solids. *Comput. Aided Des.*, 38(4):342–366, apr 2006. [1](#)
- [29] J. Stam. Exact evaluation of Catmull-Clark subdivision surfaces at arbitrary parameter values. *Proc. 25th Annu. Conf. Comput. Graph. Interact. Tech. - SIGGRAPH '98*, pages 395–404, 1998. [4](#)
- [30] J. Taylor, J. Valentin, B. Luff, R. Banks, A. Fitzgibbon, T. Sharp, E. Wood, and J. Shotton. Efficient and Precise Interactive Hand Tracking Through Joint , Continuous Optimization of Pose and Correspondences. *ACM Trans. Graph. ACM SIGGRAPH*, 35(4):143, 2016. [9](#), [10](#), [13](#), [14](#)
- [31] B. Ummenhofer and T. Brox. Global , Dense Multiscale Reconstruction for a Billion Points. *Int. Conf. Comput. Vis. Pattern Recongition*, 2015. [2](#)
- [32] W. Wang, H. Pottmann, and Y. Liu. Fitting B-spline curves to point clouds by curvature-based squared distance minimization. *ACM Trans. Graph.*, 25(2):214–238, 2006. [6](#), [9](#), [19](#)
- [33] A. Wawrzinek and K. Polthier. Computer-Aided Design Integration of generalized B-spline functions on Catmull & Clark. *Comput. Des.*, 78:60–70, 2016. [9](#)
- [34] T. Windheuser, M. Vestner, E. Rodola, R. Triebel, and D. Cremers. Optimal Intrinsic Descriptors for Non-Rigid Shape Analysis. *Br. Mach. Vis. Conf.*, page 4, 2014. [1](#)
- [35] W. Zheng, P. Bo, Y. Liu, and W. Wang. Fast B-spline curve fitting by L-BFGS. *Comput. Aided Geom. Des.*, 29(7):448–462, 2012. [9](#)